

1

2 TITLE: CARMIL3 is important for cell migration and morphogenesis during early development  
3 in zebrafish

4

5 SHORT TITLE: CARMIL3 and early development

6

7 AUTHORS: Benjamin C. Stark<sup>1</sup>, Yuanyuan Gao<sup>4</sup>, Lakyn Belk<sup>4</sup>, Matthew A. Culver<sup>4</sup>, Bo Hu<sup>4</sup>,  
8 Diane S. Sepich<sup>2</sup>, Marlene Meikel<sup>1</sup>, Lilianna Solnica-Krezel<sup>2\*</sup>, Fang Lin<sup>4\*</sup>, and John A.  
9 Cooper<sup>1,3\*</sup>.

10

11 AFFILIATIONS: <sup>1</sup>Department of Biochemistry and Molecular Biophysics, <sup>2</sup>Department of  
12 Developmental Biology, <sup>3</sup>Department of Cell Biology and Physiology, Washington University  
13 School of Medicine, St Louis, MO, <sup>4</sup>Department of Anatomy and Cell Biology, Carver College  
14 of Medicine, University of Iowa, Iowa City, IA.

15 \* Corresponding authors.

16 Email addresses for correspondence after publication: Fang Lin, [fang-lin@uiowa.edu](mailto:fang-lin@uiowa.edu);  
17 Lilianna Solnica-Krezel, [solnical@wustl.edu](mailto:solnical@wustl.edu); John Cooper, [jacooper@wustl.edu](mailto:jacooper@wustl.edu).

18

19 Contact information before publication:

20 John A Cooper  
21 CB 8231  
22 660 S. Euclid Ave.  
23 St Louis, MO 63110  
24 Phone: (314) 362-3964  
25 Email: [jcooper11@gmail.com](mailto:jcooper11@gmail.com)

## 26 Abstract

27 Cell migration is important during early animal embryogenesis. Cell migration and cell  
28 shape are controlled by actin assembly and dynamics, which depend on capping proteins,  
29 including the barbed-end heterodimeric actin capping protein (CP). CP activity can be  
30 regulated by capping-protein-interacting (CPI) motif proteins, including CARMIL (capping  
31 protein Arp2/3 myosin-I linker) family proteins. Previous studies of CARMIL3, one of the three  
32 highly conserved CARMIL genes in vertebrates, have largely been limited to cells in culture.  
33 Towards understanding CARMIL function during embryogenesis *in vivo*, we analyzed  
34 zebrafish lines carrying mutations of *carmil3*. Maternal-zygotic mutants show impaired  
35 endodermal migration during gastrulation, along with defects in dorsal forerunner cell (DFC)  
36 cluster formation, affecting the morphogenesis of Kupffer's vesicle (KV). Mutant KVs are  
37 smaller and display decreased numbers of cilia, leading to defects in left/right (L/R) patterning  
38 with variable penetrance and expressivity. The penetrance and expressivity of the KV  
39 phenotype in *carmil3* mutants correlated well with the L/R heart positioning defect at the end  
40 of embryogenesis. This first *in vivo* animal study of CARMIL3 reveals its new role for  
41 CARMIL3 during morphogenesis of the vertebrate embryo. This role involves migration of  
42 endodermal cells and DFCs, along with subsequent morphogenesis of the KV and L/R  
43 asymmetry.

44

## 45 Introduction

### 46 *CARMIL Regulation of Actin Assembly via Capping Protein*

47 CARMILs are one family of capping-protein-interacting (CPI-motif) proteins, reviewed in  
48 (Edwards et al., 2014). Vertebrates, including zebrafish, have three conserved CARMIL-  
49 encoding genes, called *CARMIL1*, *CARMIL2* and *CARMIL3* in humans (Stark et al., 2017;  
50 Stark and Cooper, 2015). The zebrafish genes, *carmil1*, *carmil2* and *carmil3*, have distinct  
51 spatial and temporal expression patterns during development (Stark and Cooper, 2015). In  
52 human cultured cells, available evidence indicates that the gene products have distinct  
53 subcellular locations and functions, even within one cell type (Lanier et al., 2015; Liang et al.,  
54 2009; Stark et al., 2017). The functions of *CARMIL1* and *CARMIL2* include cell migration,  
55 macropinocytosis, lamellipodial activity and cell polarity.

56 In contrast to this information for CARMIL1 and CARMIL2, relatively less is known about

57 the *CARMIL3* gene. In mouse, the *CARMIL3* protein localizes to developing synapses and  
58 spines in neurons, where it recruits actin capping protein. Depletion of *CARMIL3* protein in  
59 neurons leads to defects in spine and synapse assembly and function (Spence et al., 2019).  
60 In breast and prostate cancer patients, elevated expression of *CARMIL3* correlates with poor  
61 outcomes, and mouse tumor models reveal a role for *CARMIL3* in epithelial-mesenchymal  
62 transition, cadherin-based cell adhesions, and cell migration and invasion (Wang et al.,  
63 2020).

#### 64 *Cell Migration and Morphogenesis in Early Vertebrate Development*

65 Early vertebrate embryogenesis sees massive cell rearrangements that establish and  
66 shape the three germ layers, mesoderm, endoderm and ectoderm during gastrulation. The  
67 most deeply positioned endoderm gives rise to the gut and other alimentary organs. At the  
68 onset of zebrafish gastrulation, mesendodermal progenitors are located at the margin of a  
69 cup-shaped blastoderm that covers the animal hemisphere of a large yolk cell (Warga and  
70 Kimmel, 1990). The mesodermal and endodermal lineages soon separate, and internalized  
71 endodermal cells initially disperse on the yolk surface as individuals via a random walk to  
72 almost completely cover the yolk cell (Pézeron et al., 2008). Concurrently, mesoderm and  
73 ectoderm spread around the yolk cell in the process of epiboly (Warga and Kimmel, 1990).  
74 Later during gastrulation, endoderm cells migrate towards the dorsal midline along  
75 trajectories that are biased either animally/anteriorly (for cells in animal hemisphere) or  
76 vegetally/posteriorly (for cells in vegetal hemisphere), thus simultaneously elongating the  
77 nascent endoderm along the AP axis (Schmid et al., 2013). Endodermal cell migration during  
78 gastrulation depends on Rac1-regulated actin dynamics (Woo et al., 2012).

79 On the dorsal side there is a small cluster of dorsal forerunner cells (DFCs) that travel  
80 vegetalward in advance of the spreading germ layers, which later during segmentation will  
81 form an epithelial ciliated vesicle known as Kupffer's Vesicle (KV), the left-right (L/R)  
82 organizer of zebrafish (Amack and Yost, 2004). At the end of epiboly, DFCs form multiple  
83 rosette-like epithelial structures whose focal points are enriched for apical proteins. During  
84 segmentation, these rosettes arrange into a single rosette lined by a lumen with cilia at the  
85 apical membrane of the cells, thereby forming the KV (Oteíza et al., 2008). L/R patterning in  
86 zebrafish depends on the motile cilia in the KV that generate an asymmetric fluid flow (Gokey  
87 et al., 2015; Gokey et al., 2016; Sampaio et al., 2014). Mutations that affect the shape and  
88 size of the KV or that affect the number or length of cilia in the KV can impair robust L/R  
89 patterning (Amack, 2014).

90 To investigate the function of CARMIL3 in vertebrate development, we examined  
91 phenotypes resulting from the disruption of the gene encoding CARMIL3 in zebrafish. We  
92 found defects in endodermal cell migration, DFC migration and clustering, KV  
93 morphogenesis, the number of cilia in the KV, and L/R asymmetry.

## 94 Materials & Methods

### 95 *Zebrafish lines and husbandry*

96 Animal protocols were approved by the Institutional Animal Care and Use Committees  
97 at University of Iowa and Washington University. At University of Iowa, zebrafish were  
98 maintained as described previously (Xu et al., 2011) and embryos were obtained by natural  
99 spawning and staged according to morphological criteria or hours post fertilization (hpf) at  
100 28°C or 32°C unless otherwise specified, as described previously (Kimmel et al., 1995). At  
101 Washington University, zebrafish and embryos are maintained at 28.5°C using the standard  
102 operating procedures and guidelines established by the Washington University Zebrafish  
103 Facility, described in detail at <http://zebrafishfacility.wustl.edu/documents.html>. The following  
104 zebrafish lines were used in this study: AB\*/Tuebingen, *Tg(sox17:EGFP)* (Mizoguchi et al.,  
105 2008), *carmil3<sup>sa19830</sup> (lrrc16b<sup>sa19830</sup>)*, and *carmil3<sup>stl413</sup>*.

106 Zebrafish line *carmil3<sup>sa19830</sup> (lrrc16b<sup>sa19830</sup>)* was obtained from the Zebrafish International  
107 Resource Center (Eugene, OR) (described at <https://zfin.org/ZDB-ALT-131217-14950>)  
108 (Kettleborough et al., 2013). The mutation was created by *N*-ethyl-*N*-nitrosourea (ENU)  
109 treatment of adult males, and the mutated gene has a G to T conversion at an essential  
110 splice site of intron 27-28, which introduces multiple stop codons beginning at amino acid  
111 residue 832 (Kettleborough et al., 2013). Failure to splice at this site is predicted to change  
112 amino-acid residue 831 from E to D, with the next codon being ochre TAA, and thus  
113 truncating the protein to 832 residues from its normal length of 1384 residues. Zebrafish line  
114 *carmil3<sup>stl413</sup>* was produced via TALEN-mediated mutagenesis (Boch et al., 2009; Moscou and  
115 Bogdanove, 2009). TALEN sequences used were 5'-TGACAAGACATCAATCAAGT and 5'-  
116 TTTGCCACTCTTGTCTCTG (corresponding to bases 72063-72082 and 72101-72120,  
117 respectively, of the sequence for the genomic locus FQ377660). TALEN cleavage led to  
118 several different independent mutations in founder fish. The largest deletion was of an 11-bp  
119 segment of exon 2, 5'-ACGTATCAAAG. This deletion eliminates the Alu1 restriction site  
120 found in exon 2, and the deletion leads to a premature stop codon at amino-acid residue 101.  
121 Fish carrying this mutation were selected for outcrossing and further study.

122 *carmil3*<sup>sa19830</sup> and *carmil3*<sup>stl413</sup> were genotyped by restriction enzyme digestion of PCR  
123 amplicons containing the mutations. For *carmil3*<sup>sa19830</sup> the forward primer was 5'-  
124 AGCAGAGTGTCTTTCTCCAC, and the reverse primer was 5'-  
125 GATCGAGGTTGGAGGTGAAC. MseI digest distinguished WT (191 bp band) from *sa19830*  
126 mutant (bands at 123 bp and 38 bp). For *carmil3*<sup>stl413</sup> the forward primer was 5'-  
127 AGAATAGTGTAATCCACTCATTTCACCG, and the reverse primer was 5'-  
128 AGGCAGGTGTGAATACCTTTAAAGTCTTCA (corresponding to bases 71935-71965 and  
129 72249-72278, respectively, of the sequence for the genomic locus FQ377660). AluI digestion  
130 produced two bands at 157 bp and 187 bp from WT genomic DNA, and a single band at 333  
131 bp from the mutant. Mutant founders were outcrossed into WT AB fish to produce  
132 heterozygous fish, which were fully viable, and they were mated to produce maternal and  
133 maternal-zygotic homozygous mutants. Alternatively, genotyping of *carmil3*<sup>sa19830</sup> mutants  
134 was performed by Transnetyx (Cordova, TN) using real-time PCR with allele-specific probes.

### 135 *Protein expression and purification*

136 Capping protein (CP, mouse alpha1beta2) was expressed and purified as described  
137 (Johnson et al., 2018). Glutathione-S-transferase (GST)-tagged CP binding region (CBR)  
138 fragments of human CARMIL1a (E964-S1078, plasmid pBJ 2411), human CARMIL3 (S955-  
139 S1063, plasmid pBJ 2449), zebrafish Carmil3 (S943-N1040, plasmid pBJ 2451) and  
140 zebrafish Carmil3 CPI-mutant (S943-N1040, with point mutations H944A and R966A, plasmid  
141 pBJ 2452) were expressed from pGEX-KG vectors in *E. coli* BL21 Star (DE3). The fusion  
142 proteins were affinity-purified on Glutathione Sepharose® 4 Fast Flow (GE Healthcare), and  
143 then bound to POROS GoPure XS (Applied Biosystems) in 20 mM NaH<sub>2</sub>PO<sub>4</sub>, 100 μM EDTA,  
144 1 mM NaN<sub>3</sub>, 5 mM DTT, 4M urea (pH 7.5). After elution with a gradient to 1 M NaCl in the  
145 same buffer, the purified GST-CBR fragments were concentrated and stored at -70°C.

### 146 *Actin polymerization assays*

147 Pyrene-actin polymerization assays were performed as described (Carlsson et al.,  
148 2004). Pyrene-labeled and unlabeled gel-filtered rabbit muscle actin stocks were mixed to  
149 produce a total actin monomer concentration of 1.5 μM in the cuvette. Pyrene-actin filament  
150 seeds were prepared as described (Ramabhadran et al., 2012). CP at 5 nM and GST-CBR at  
151 varied concentrations were added at the start of the experiment (0 sec). Pyrene-actin  
152 fluorescence was measured using time-based scans on a steady-state fluorometer  
153 (QuantaMaster, PTI, Edison, NJ) with excitation at 368 nm and emission at 386 nm.

154 *Whole-mount RNA in situ hybridization (WISH)*

155 Digoxigenin-labeled antisense RNA probes for *myl7* (cardiac myosin regulatory light  
156 chain) (Ye and Lin, 2013; Yelon et al., 1999), *sox17* (sex determining region Y-box 17)  
157 (Alexander et al., 1999; Hu et al., 2018), *southpaw* (*spaw*) (Long et al., 2003; Panizzi et al.,  
158 2007) were synthesized by *in vitro* transcription. Staged embryos were fixed in 4% fish fix  
159 solution (4% paraformaldehyde, 4% sucrose, 0.1 M phosphate buffer pH 7.2, 0.12 mM CaCl<sub>2</sub>)  
160 at 4°C overnight. Fixed embryos were manually dechorionated and dehydrated with a series  
161 of methanol washes. WISH was performed as described (Thisse and Thisse, 2008).

162 *Whole-mount Immunofluorescence*

163 Staged embryos (10-14 somites) were manually dechorionated and fixed in Dent's  
164 fixative (80% methanol: 20% DMSO) at room temperature for a minimum of 2 hrs. Antibody  
165 staining was performed in PBDT (1% BSA, 2% goat serum, 2% DMSO, 0.1% Triton X-100 in  
166 PBS) as described (Topczewski et al., 2001; Ye and Lin, 2013). The following antibodies  
167 were used: mouse anti-acetylated tubulin (clone 6-11b-1, Sigma-Aldrich, diluted 1:2000) and  
168 goat anti-mouse Alexafluor 488 (Invitrogen, diluted 1:2000).

169 *Microscopy and Image Analysis*

170 WashU: For Figure 4 D-G, fluorescence images were collected on a spinning disk  
171 confocal microscope (Quorum, Canada) using an inverted Olympus IX-81 microscope, a  
172 Hamamatsu EMCCD camera (C9100-13) and Metamorph acquisition software. For Figures  
173 2A, 5, and 6, WISH images were collected on a Nikon Macroscope with a Nikon AZ100  
174 objective, a 1x lens N.A. 0.1, and a 4x lens N.A. 0.4.

175 Iowa: For still epifluorescence images, live or fixed embryos were mounted in 2%  
176 methylcellulose and photographed using a Leica DMI 6000 microscope with a 5×/NA 0.15  
177 objective or a 10×/NA 0.3 objective. For ISH images in Figure 3, embryos were mounted in  
178 80% glycerol/PBS and photographed using a Leica M165FC Stereomicroscope with a Leica  
179 DFC290 Color Digital Camera.

180 For time-lapse imaging of endodermal cells in Figure 2 C-G and Figure 4 A-C,  
181 *Tg(sox17:EGFP)* embryos were embedded in 0.8% low-melting agarose in a dorsal-mount  
182 imaging mold as previously described (Ye et al., 2015). Time-lapse imaging was taken in the  
183 dorsal region of endoderm at 25°C, at 5-minute interval with a 5×/NA 0.15 objective on an  
184 inverted Leica DMI 6000 microscope. Images were processed and cell tracking analyzed

185 using ImageJ (Schneider et al., 2012). Data were exported to Excel where cell migration  
186 speed, paths, direction were determined as previously reported (Lin et al., 2005).

### 187 *Statistical Analysis*

188 Data were compiled from two or more independent experiments and were presented  
189 as the mean  $\pm$  SEM or  $\pm$  SD as indicated in figure legends. Statistical analyses were  
190 performed in GraphPad Prism (GraphPad Software) using unpaired two-tailed Student's *t*-  
191 tests with unequal variance. The numbers of cells and embryos analyzed in each experiment  
192 and significance levels are indicated in graphs and/or the figure legends.

193

## 194 **Results**

195 As part of our interest in how actin assembly and actin-based motility contributes to  
196 morphogenesis and cell movement during development, we examined the role of CARMIL3.  
197 The CARMIL family of proteins regulate the heterodimeric actin capping protein (CP) that  
198 controls polymerization of actin filaments at barbed ends, *in vitro* and in cells (Stark et al.,  
199 2017). To advance our understanding of the functions of the three CARMIL isoforms  
200 conserved across vertebrates, we first assayed biochemical activities of zebrafish *Carmil3* in  
201 comparison to human CARMIL3 and CARMIL1. Second, we altered the activity of the  
202 zebrafish *carmil3* gene, previously known as *lrrc16b* and *si:ch211-204d18.1*, by creating  
203 and/or interrogating lines carrying homozygous loss-of-function mutations.

204

### 205 *CARMIL3 inhibits actin capping activity of CP*

206 The biochemical activities of the vertebrate CARMIL1 and CARMIL2 isoforms with  
207 respect to CP and actin have been studied in mouse and human systems (Stark et al., 2017).  
208 The ~100-aa capping protein binding region (CBR) of CARMIL1 and CARMIL2 are known to  
209 bind directly to CP and partially inhibit its actin capping activity, via an allosteric mechanism.  
210 Comparative studies of CARMIL3 had not been previously done and so we performed them  
211 here.

212 We prepared recombinant proteins corresponding to the CBR region of CARMIL3 from  
213 human and zebrafish, and we tested their ability to inhibit the capping activity of mouse non-  
214 sarcomeric CP ( $\alpha$ 1 $\beta$ 2) (Edwards et al., 2013). In actin polymerization assays seeded  
215 with barbed ends of actin filaments, CP inhibited actin polymerization (Fig. 1A). A human

216 CARMIL3 (C3) CBR fragment partially reversed the inhibitory effect of CP, with a potency  
217 slightly greater than that of human CARMIL1 (C1) (Fig. 1A). Zebrafish Carmil3 (C3) CBR also  
218 inhibited CP (Fig. 1B), with a potency approximately half that of human CARMIL3. Specific  
219 point mutations known to impair the ability of human CARMILs to interact with CP (Edwards  
220 et al., 2013; Lanier et al., 2015) were also created in the CBR fragment of zebrafish Carmil3  
221 (C3-HRAA). The mutant CBR failed to inhibit CP activity (Fig. 1 B). Thus, the CBR region of  
222 CARMIL3, from both human and zebrafish, is able to inhibit the capping activity of CP, in a  
223 manner consistent with the direct-binding mechanism described for other CARMILs (Stark et  
224 al., 2017). This result supports the hypothesis that functional properties of CARMIL3 in  
225 vertebrates may involve direct interaction with CP.

226

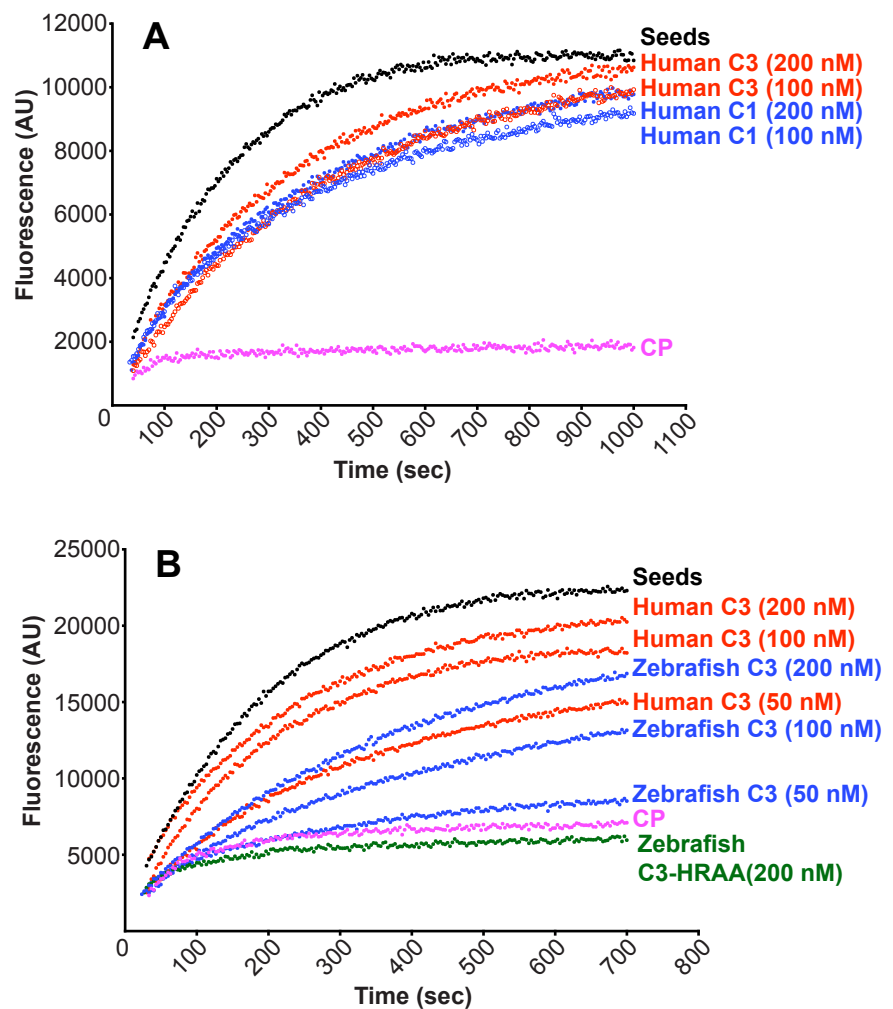
227 **Figure 1.** CARMIL3 inhibits capping protein (CP) activity in actin polymerization assays, with  
228 pyrene-actin fluorescence (arbitrary units) plotted vs time. A) Human CARMIL3 (C3) inhibited  
229 the ability of CP to cap barbed ends of actin filaments. Black points, labeled “Seeds,” are  
230 from a control with

231 monomeric actin and  
232 filamentous actin seeds.  
233 Pink points, labeled “CP,”  
234 correspond to a sample to  
235 which CP was added. Red  
236 and blue curves contain  
237 CP plus the indicated

238 concentrations of human  
239 CARMIL1 or CARMIL3

240 CBR fragment. B)

241 Zebrafish CARMIL3 (C3,  
242 blue curves) inhibited  
243 capping by CP. In  
244 comparison to human  
245 CARMIL3 (C3, red curves),  
246 the inhibitory activity of  
247 zebrafish CARMIL3 was  
248 slightly less than that of





249 human CARMIL3, based on similar concentrations as indicated. A mutant form of zebrafish  
250 CARMIL3 (C3-HRAA, green curve) containing two point mutations at conserved residues of  
251 the CP-binding CPI motif, failed to block CP activity, as expected.

252

### 253 *Genomic mutations of zebrafish carmil3: Creation and characterization*

254 A *carmil3* mutant line from the Zebrafish Mutation Project (Kettleborough et al., 2013),  
255 *carmil3<sup>sa19830</sup>*, carries a single-nucleotide change at an essential splice site, predicted to  
256 truncate the protein to 832 residues from its WT length of 1384 residues. We created a  
257 second *carmil3* mutant line by TALEN-mediated mutagenesis, *carmil3<sup>stl413</sup>*; this mutation  
258 produces an 11-bp deletion within exon 2 that causes a frameshift followed by a nonsense  
259 mutation, predicted to produce a truncated protein of 101 residues. Heterozygous and  
260 homozygous zygotic mutants of both alleles were viable as embryos and adults and did not  
261 present any overt phenotypes. When fish homozygous for either of the two alleles were  
262 crossed, the resulting embryos, deficient in both maternal and zygotic *carmil3* function,  
263 MZ*carmil3<sup>sa19830/sa19830</sup>* (thereafter MZ*carmil3<sup>sa19830</sup>*) or MZ*carmil3<sup>stl413/413</sup>* (thereafter  
264 MZ*carmil3<sup>stl413</sup>*), also completed epiboly and gastrulation and developed into morphologically  
265 normal embryos.

266

### 267 *Migration of endodermal cells*

268 To assess potential subtle or transient developmental defects, we analyzed the  
269 expression of germ layer markers in MZ*carmil3* mutants at mid-gastrulation by whole mount  
270 *in situ* hybridization (WISH). We examined the positions of endodermal cells and DFCs,  
271 marked by expression of *sox17*, over time during gastrulation. In embryos fixed and stained  
272 by whole-mount *in situ* hybridization (WISH) at midgastrulation (70-80% epiboly), we noted  
273 that the leading edge of the vegetally migrating endodermal cells in MZ*carmil3<sup>sa19830</sup>* mutant  
274 embryos lagged behind that of WT embryos (Fig. 2A). To quantify the effect, we measured  
275 the distance from the front edge of the endodermal cells to the edge of the aggregation of  
276 DFCs, as diagrammed on the right side of Figure 2B. The distance was larger for the  
277 MZ*carmil3<sup>sa19830</sup>* mutant, compared to WT embryos (Fig. 2B), indicating that *carmil3* is  
278 important for endodermal migration. The mean distance values were 67  $\mu\text{m}$  (95% confidence  
279 interval of 60-74, n=61) for WT embryos and 142  $\mu\text{m}$  (95% confidence interval of 135-150,  
280 n=55) for mutant embryos. The difference between the two sets of data had a two-tailed P

281 value of <0.0001 in an unpaired t test. These data were combined from clutches obtained on  
282 separate days.

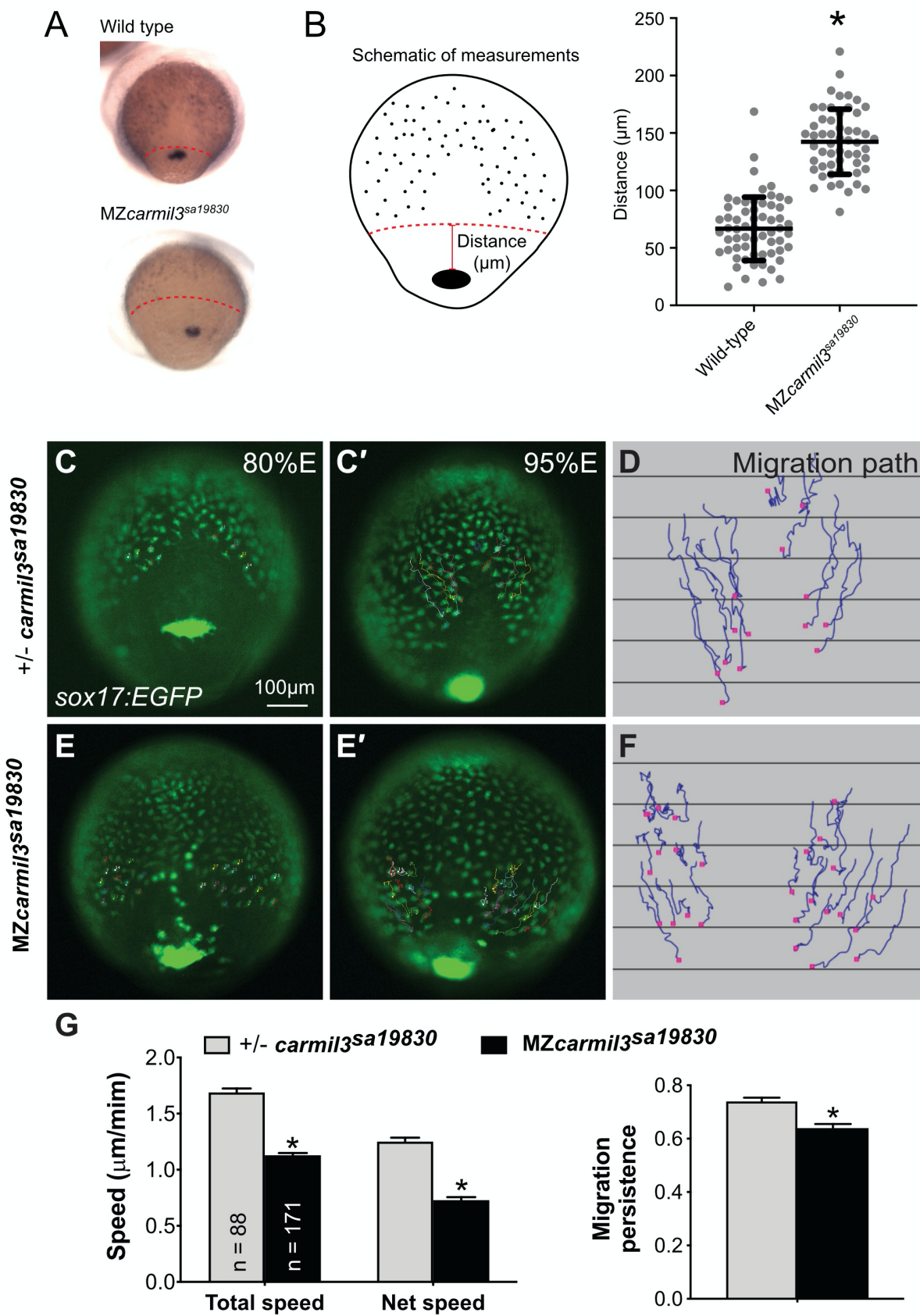
283

284

285

286 **Figure 2.** Pattern of endodermal cell migration in *carmil3* mutant embryos compared to WT  
287 embryos. Panels A and B are results from *sox17* staining of embryos at 70-80% epiboly. A.  
288 Representative images illustrating the patterns observed in WT compared to MZ*carmil3*<sup>sa19830</sup>  
289 mutant embryos. Red dotted line indicates the margin of the endoderm, used to measure  
290 migration distance. B. Endodermal cell migration distribution, measured as illustrated in the  
291 schematic and the images of panel A. In the plot, each data point corresponds to one  
292 embryo. Values for the distributions were as follows (mean ± s.d.): WT 74 ± 25 (N=50),  
293 MZ*carmil3*<sup>sa19830</sup> mutant 144 ± 28 (N=44). Asterisk (\*) indicates p value of <0.0001 in  
294 Student's *t*-test. Panels C through G are results from epifluorescence time-lapse experiments  
295 performed on MZ*carmil3*<sup>sa19830</sup> or MZ*carmil3*<sup>sa19830</sup> mutant embryos, each carrying  
296 *Tg(sox17:EGFP)/+*. (C and E) Snapshots at 80% epiboly stage from the time-lapse movie,  
297 with the tracked cells labeled. (C' and E') Snapshots at 95% epiboly stage, with the migration  
298 tracks of endodermal cells from the 80% to 95% epiboly stage superimposed. Scale bar:  
299 100µm. (D, F) Migration tracks delineate routes of endodermal cells. Solid magenta squares  
300 denote the endpoint of migration. (G) Total speeds, net speeds, and migration persistence.  
301 The number of cells analyzed is indicated in the first graph. Asterisk (\*) indicates p value of  
302 <0.0001 in Student's *t*-test.

303



306 To test this observation directly in living embryos, we then examined the migration of  
307 the endodermal cells by conducting fluorescence microscopy time-lapse analyses using a  
308 transgenic line expressing eGFP fluorescent protein from the *sox17* gene promoter  
309 *Tg(sox17-GFP)* (Fig. 2) (Mizoguchi et al., 2008). Cell tracking revealed that in control  
310 embryos (heterozygous *carmil3<sup>sa19830/+</sup>*), endodermal cells migrate toward the vegetal pole  
311 and converge dorsally along fairly straight paths (Schmid et al., 2013) (Fig. 2C-D). In  
312 contrast, in *carmil3*-deficient mutants (*MZcarmil3<sup>sa19830</sup>*) the endodermal cells took less direct  
313 paths (Fig. 2E-F). Further cell tracking analyses showed that both cell movement, i.e. (total  
314 speed: movements in all directions) and migration efficiency (net speed: along straight line  
315 between the start and endpoint) were impaired in mutants compared to WT controls, as was  
316 the persistence of migration (ratio of net : total speed) (Fig. 2G). Thus, Carmil3 is required for  
317 efficient migration of endodermal cells.

318

#### 319 *Aggregation of dorsal forerunner cells (DFC)*

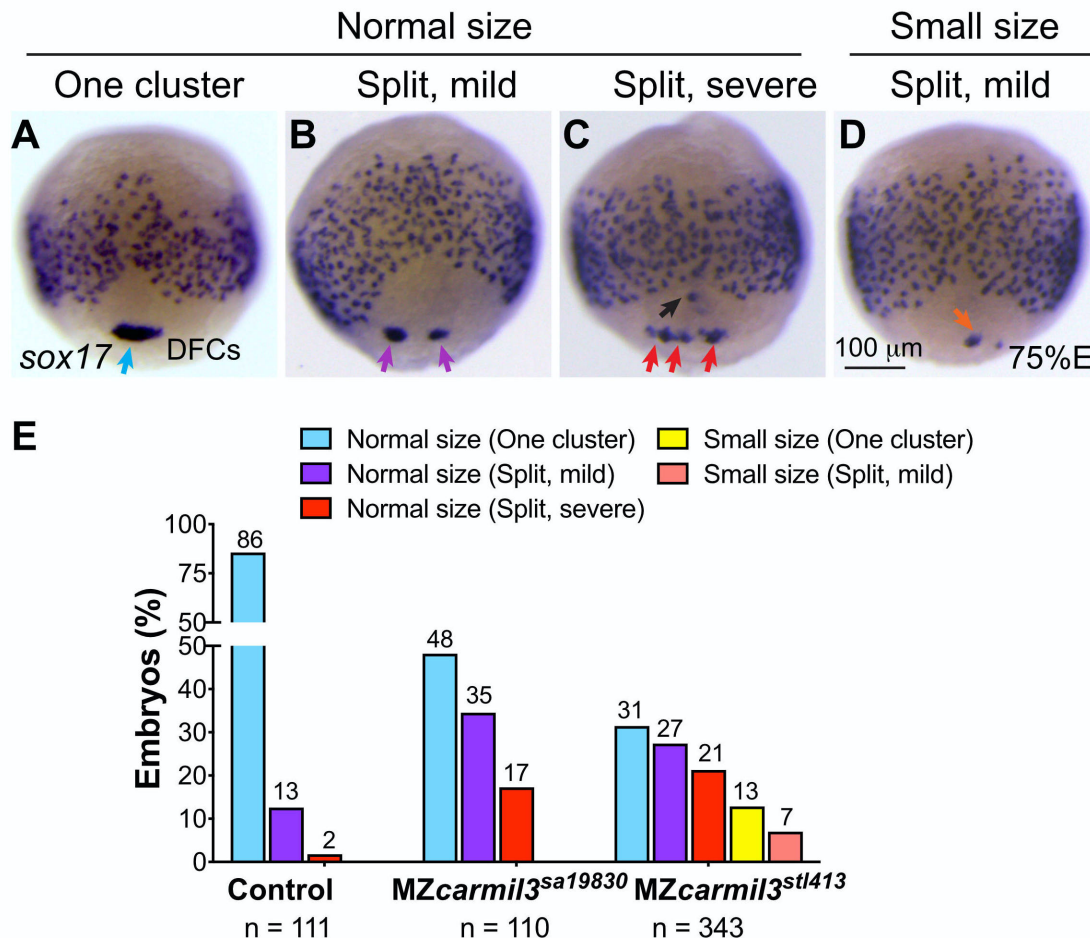
320 Static images from these time-lapse experiments with a *Tg[sox17:EGFP]* background  
321 also revealed the migration and cluster formation by dorsal forerunner cells (DFCs), which  
322 strongly expressed eGFP. DFCs in WT embryos usually formed a single large cluster (Fig.  
323 2C). In mutant embryos, the DFC cluster was fragmented; we observed this in  
324 *MZcarmil3<sup>sa19830</sup>* embryos (Fig. 2E) and in *MZcarmil3<sup>stl413</sup>* mutant embryos (data not shown).  
325 In addition, we noted bright GFP-labeled cells that resided in an apparent gap between the  
326 DFC cluster and the leading edge of the migrating endodermal cells (Fig. 2E) in the mutant,  
327 but not WT embryos, which we suggest correspond to DFCs exhibiting abnormal migration.

328 We further examined DFC cluster morphology and DFC distribution during gastrulation  
329 using WISH probes for cells expressing *sox17*; these results also revealed the location of  
330 DFCs over time in larger populations of WT and mutant embryos. We examined embryos at  
331 70-80% epiboly (midgastrulation; Fig. 3), and we observed variation in the size and  
332 coherence of the DFC cluster in the mutants compared to WT. To score the phenotype, we  
333 graded the morphology of the aggregated set of DFCs as “normal size, one cluster;” “normal  
334 size, split-mild,” “normal size, split-severe;” “small size, one cluster,” and “small size, split-  
335 mild.” Representative images are shown in Figure 3A-D, and graphs with quantification of  
336 these results, for control, *MZcarmil3<sup>sa19830</sup>*, and *carmil3<sup>stl413</sup>* mutant embryos, are presented in  
337 Fig. 3E. These results corroborate the observations from the time-lapse analyses, showing

338 that formation of a cohesive DFC cluster is impaired in *carmil3*-deficient gastrulae, which  
 339 frequently displayed a fragmented and/or smaller DFC aggregate.

340

341 **Figure 3.** Patterns of dorsal forerunner cell (DFC) distribution in *MZcarmil3<sup>sa19830</sup>* mutant  
 342 embryos compared to heterozygous +/ *MZcarmil3<sup>sa19830</sup>* embryos. Panels A to D illustrate the  
 343 patterns observed, with results quantified in panel E. In most embryos, DFCs form a single  
 344 tight cluster of normal size (light blue arrow in panel A and light blue bars in panel E). In some  
 345 embryos, DFCs display three patterns of defects: B) normal size with mild splitting (i.e. two  
 346 clusters); C) normal size with severe splitting (more than two clusters), and D) small size with  
 347 mild splitting. (E) Percentages of embryos displaying the patterns of DFC defects in both  
 348 *MZcarmil3<sup>sa19830</sup>* and *MZcarmil3<sup>stl413</sup>* mutants. The percentage of embryos in each group is  
 349 indicated above each bar, and the total number of embryos in each group (N) is listed  
 350 underneath the labels on the abscissa.



351

352 *Morphology of the Kupffer's Vesicle and Cilia*

353 The cluster of DFCs that forms during gastrulation, undergoes a morphogenetic  
354 transition into an epithelial sac known as Kupffer's Vesicle (KV), the ciliated organ that  
355 determines L/R asymmetry during zebrafish development (Gokey et al., 2016). Because we  
356 observed a defect in DFC aggregate formation, we examined the morphology of the KV and  
357 its cilia during segmentation (Fig. 4).

358 Imaging the KV in *MZcarmil3<sup>stl413</sup>* mutant (*Tg[sox17:EGFP]*) embryos at the 6-somite  
359 stage (Fig. 4A,B,B'), revealed that their KV during early segmentation was significantly  
360 smaller than in control WT embryos (Fig. 4C). To visualize the epithelial KV morphology  
361 during later development, we stained embryos fixed at the stage of 10-14 somites with  
362 antibodies against the epithelial marker atypical PKC (aPKC) (Amack et al., 2007) and  
363 acetylated tubulin (Ac-tubulin) (Piperno and Fuller, 1985), resolving the cilia as individual  
364 structures, allowing us to count their number and measure their length. In these images, the  
365 hollow empty center of the KV appears as a relatively dark unstained region in the aPKC  
366 channel and as staining positive for cilia in the Ac-tubulin channel. In instances where the KV  
367 did not "inflate" (*MZcarmil3<sup>sa19830</sup>* in Fig. 4D, bottom panel), an unstained region was not  
368 observed. As in earlier stages, the KV was often smaller or fragmented, resulting in a  
369 decreased KV area for both mutants (Fig. 4C and 4E). The decrease in KV area was  
370 statistically significant (Fig. 4E), and the magnitude of the decrease was sufficiently large that  
371 the values were at or below the value for the area of the KV at this stage found to be  
372 necessary for robust L/R patterning by Gokey and colleagues (Gokey et al., 2016), which is  
373 drawn as a dotted line at 1300  $\mu\text{m}^2$  in Figure 4E.

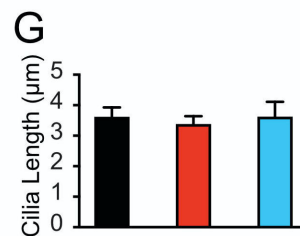
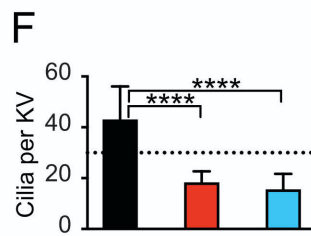
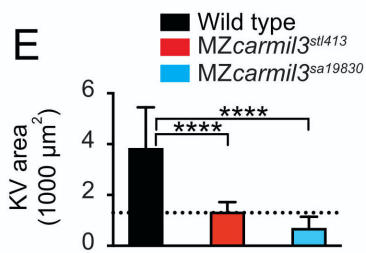
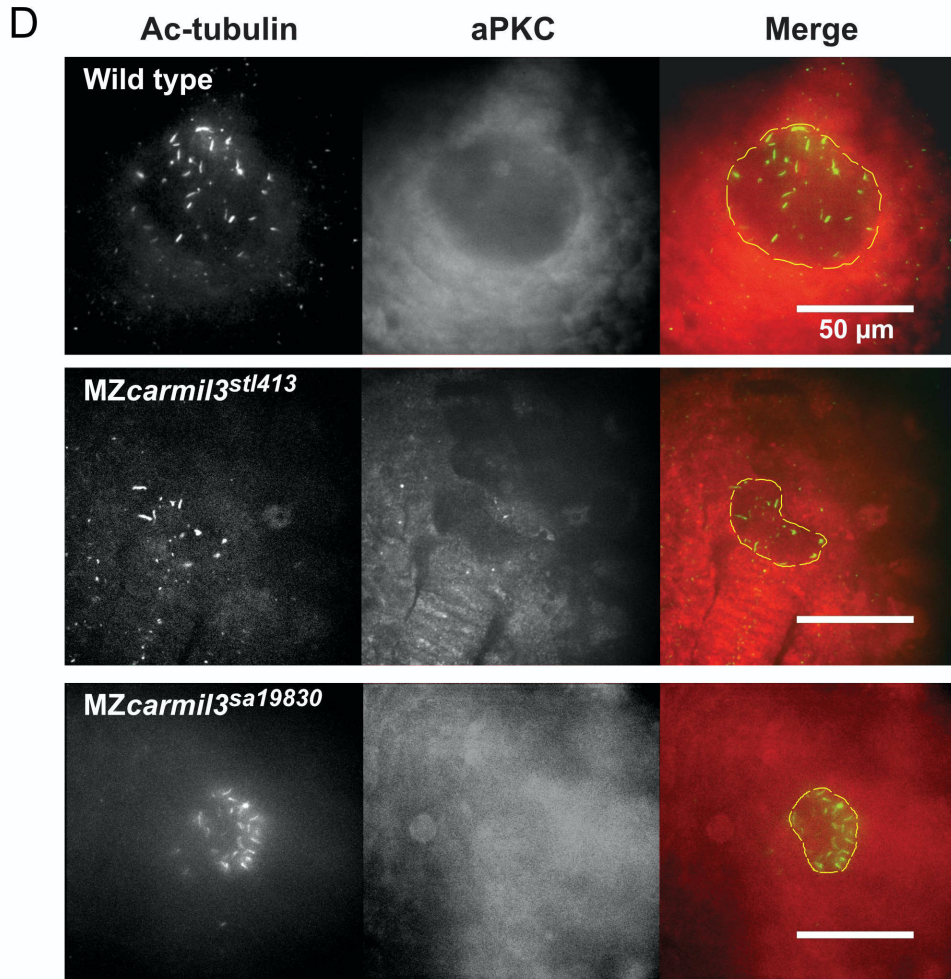
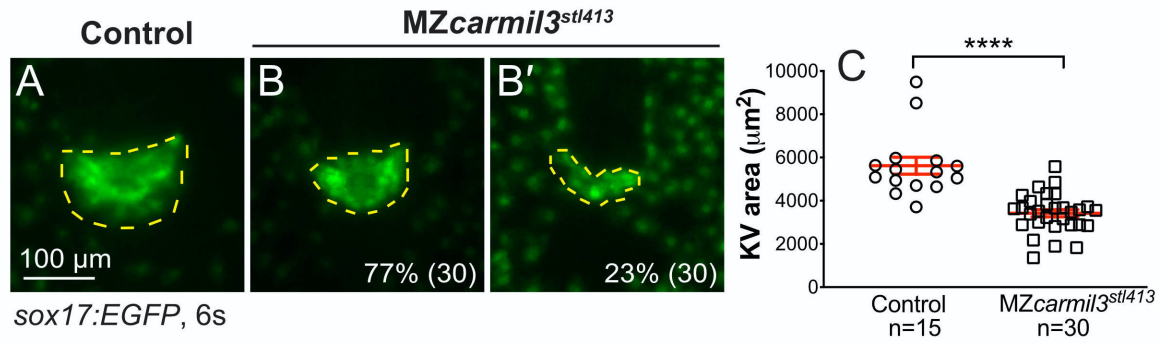
374 We analyzed the cilia in greater detail, and found that the number of cilia per KV was  
375 decreased in both mutants (Fig. 4F). The decreases were substantial and significantly  
376 different from WT embryos. In Figure 4F, the dotted line at 30 cilia per KV corresponds to the  
377 value that was found to be necessary for robust L/R patterning by Sampaio and colleagues  
378 (Sampaio et al., 2014). In both mutants, the number of cilia per KV was below this threshold  
379 (Fig. 4F). In contrast, the length of the cilia did not differ in the mutant embryos compared to  
380 WT embryos (Fig. 4G), suggesting that *Carmil3* is not required for cilia biogenesis per se, but  
381 instead plays a role in the size and/or morphology of the KV.

382

383

384 **Figure 4.** Morphology of Kupffer's vesicle (KV) and cilia in *carmil3* mutant embryos. Panels A  
385 through C are from one analysis, based on wide-field fluorescence images showing the  
386 morphology of *sox17*-EGFP labelling of the KV in control (A) and MZ*carmil3*<sup>stl413</sup> mutant (B-  
387 B') embryos at the 6-somite stage. (C) Area of the KV in control and MZ*carmil3*<sup>stl413</sup> mutant  
388 embryos. All the data points are shown. The red lines indicate the mean and one standard  
389 error of the mean. The results are statistically significant with a p value of < 0.0001. The  
390 number of embryos analyzed was 15 for control and 30 for mutant. In this set of experiments,  
391 the control was a heterozygous strain. Panels D through G are from a second experimental  
392 series with a different set of animals, based on confocal images of embryos at the 10-14  
393 somite stage stained to visualize cilia and the KV, with antibodies to acetylated tubulin (Ac-  
394 tubulin, Green in Merge), and to atypical PKC (aPKC, Red in Merge) respectively. With anti-  
395 aPKC staining, the KV appears as a relatively dark area, owing to the absence of cells inside  
396 the vesicle. WT and two different *carmil3* mutant embryo lines are shown. The Merge panel  
397 shows examples of how the KV was outlined for calculation of area; the outline is based on  
398 both Ac-tubulin and aPKC images. Panels E through G are graphs of parameters quantified  
399 from the images, with the color scheme for WT and mutants as indicated. In each panel, the  
400 plotted values are the mean, and the error bars correspond to one standard deviation. E)  
401 Area of the KV. Horizontal dotted line corresponds to the value for area of KV found to be  
402 necessary for robust L/R patterning by Gokey and colleagues (Gokey et al., 2016). Values for  
403 the two mutants differ from the value for WT based on Student's t-test ( $p < 0.005$   
404 (actual=0.0006 and 0.0005)). F) Number of cilia per KV. Horizontal dotted line corresponds to  
405 the value for number of functional cilia per KV (30) found to be necessary for robust left / right  
406 patterning by Sampaio and colleagues (Sampaio et al., 2014). Values for the two mutants  
407 differ from the value for wild type based on Student's t-test ( $p < 0.005$  (Actual=0.0001 and  
408 0.0004)). G) Length of cilia. Values for the two mutant lines do not differ from the value for  
409 WT embryos based on Student's t-test ( $p = 0.3277$  and  $> 0.9999$ ). Values of N as in panel E.  
410 Values of N (embryos counted) as follows: WT, 9; MZ*carmil3*<sup>stl413</sup>, 8; MZ*carmil3*<sup>sa19830</sup>, 4 for  
411 panels to G.

412





413 *Left-Right Patterning*

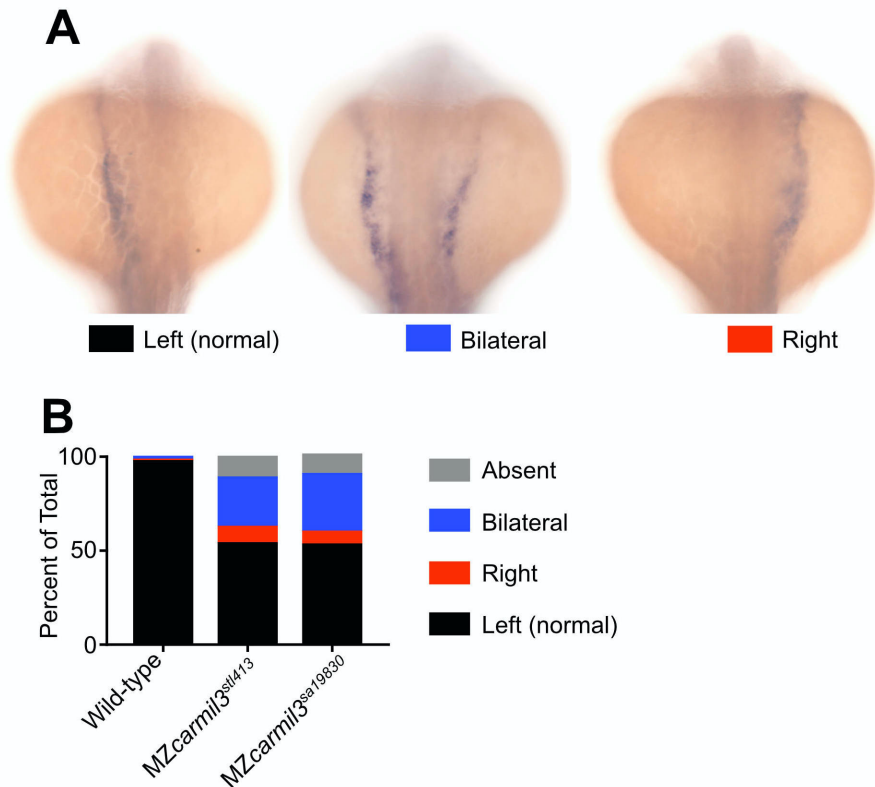
414 Because we observed defects in formation of the KV, including its morphology, size  
415 and the number of cilia; we asked whether further development revealed defects in L/R  
416 asymmetry pathways and outcomes. Since the *carmil3* mutants displayed the KV area and  
417 number of cilia below the thresholds shown to be required for robust L/R patterning by  
418 previous studies (Gokey et al., 2016; Sampaio et al., 2014), we hypothesized that there  
419 would be defects in L/R patterning in these mutants.

420 First, we examined the pattern of expression of the lateral plate mesoderm marker  
421 *southpaw* (*spaw*) in embryos at the 18-20 somite stage (Fig. 5) (Long et al., 2003). Whereas  
422 WT embryos uniformly displayed *spaw* staining on the left, the two *carmil3* mutant lines  
423 showed substantial percentages of embryos with bilateral or right-sided *spaw* staining.  
424 Representative examples are shown in panel A of Figure 5, with quantitation in panel B and  
425 Table I. Results for the two mutant lines were similar to each other and differed significantly  
426 from results for WT embryos. These embryos were generated from the same set of mutant  
427 and WT animals as those used in the experiments illustrated in panels D-G of Figure 4,  
428 where the KV area and number of cilia per KV were below the critical threshold in the mutant.  
429 When a different generation of mutant animals was used in a separate set of experiments to  
430 generate MZ*carmil3*<sup>stl413</sup> embryos, in which the KV area was not below the critical value  
431 illustrated in panels A-C of Figure 4, little or no defects in *spaw* staining distribution were  
432 observed (data not shown), consistent with the findings of Gokey and colleagues (Gokey et  
433 al., 2016), and Sampaio and colleagues (Sampaio et al., 2014) noted above.

434

435 **Figure 5.** Patterns of *spaw* staining distribution at the 18-20 somite stage in *carmil3* mutant  
436 embryos compared with WT embryos. A. Representative images illustrate observed patterns  
437 of *spaw* staining, which is purple. B. Percentage of *spaw* staining patterns, comparing WT  
438 embryos with embryos of two different *carmil3* mutant lines, MZ*carmil3*<sup>stl413</sup> and  
439 MZ*carmil3*<sup>sa19830</sup>. The color scheme is indicated in panel A, below the images. In cases  
440 scored as “absent,” no staining was observed. Values are listed in Table I.

441

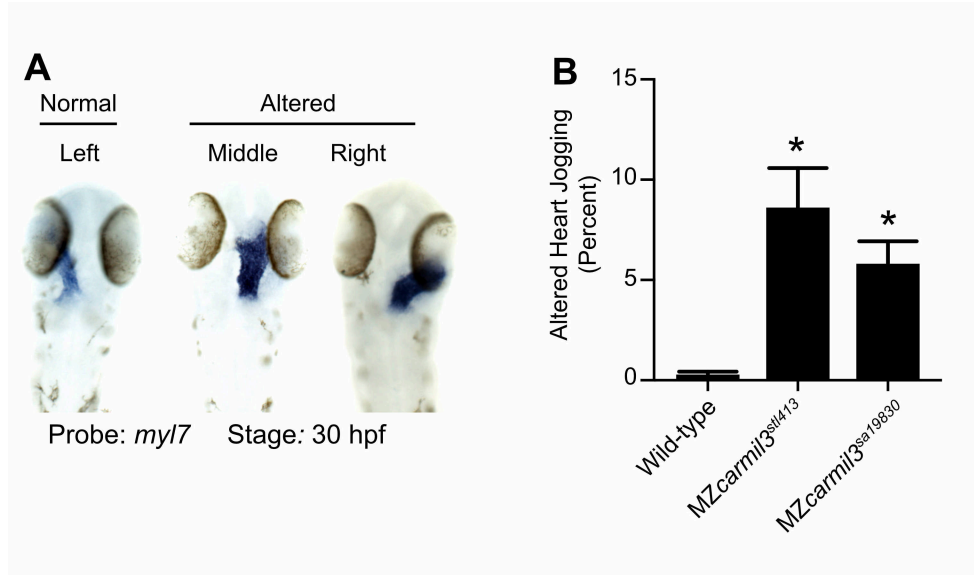


442

443 *spaw* regulates FGF signaling (Neugebauer and Yost, 2014), and *spaw* mutants are  
444 defective in L/R asymmetry, as revealed by the position of the heart (Ahmad et al., 2004;  
445 Long et al., 2003). Therefore, we asked whether mutant embryos had a phenotype related to  
446 heart position. Indeed, mutant embryos at ~30 hpf displayed a defect in the L/R positioning of  
447 the heart (Fig. 6). In a noticeable and significant number of embryos, the heart was in the  
448 middle or on the right side of the embryo, based on staining for cardiac myosin light chain  
449 (*myl7*), for which representative examples are shown in panel A of Figure 6. A combined  
450 count of embryos with altered heart position showed defects of 6 - 9% for each of the two  
451 mutants and a value less than 1% observed in WT embryos (Fig. 6, Panel B). The defects in  
452 the two mutant lines did not differ from each other by a statistically significant degree, and the  
453 differences between the two mutant lines and the WT line was highly significant in both  
454 cases.

455

456 **Figure 6.** Heart position in *MZcarmil3* mutant embryos compared to WT embryos at ~30 hpf,  
457 assessed by staining for transcripts of *myl7*, the gene encoding cardiac myosin light chain, in  
458 blue. A. Representative images illustrate observed patterns. B. Quantification of the sum of  
459 the two altered patterns, termed “heart jogging,” in two different *MZcarmil3* mutant embryo  
460 lines compared with WT embryos. WT embryos displayed the abnormal (to the right or  
461 center) heart jogging phenotype 0.25% of the time (N=784). This value was significantly  
462 higher in the mutant embryos: 8.6% for *MZcarmil3<sup>stl413</sup>* (N=198) and 5.8% for *MZcarmil3<sup>sa19830</sup>*  
463 (N=415). Error bars  
464 indicates standard  
465 error of proportion. P  
466 values were calculated  
467 from Fisher’s exact test  
468 calculated with  
469 GraphPad Prism.  
470 Asterisk indicate that  
471 for both mutants,  
472 compared with WT, p  
473 values were <0.0001.



474

475 As above for *spaw* staining, these data for heart position are from a set of animals and  
476 experiments where the KV area and number of cilia per KV in the mutant were below the  
477 critical threshold (Fig. 4 D-G). In a separate set of experiments, using *MZcarmil3<sup>stl413</sup>*  
478 mutants, in which the KV area was not below the critical value (Fig. 4 A-C), little or no defects  
479 in heart position were observed (data not shown). Therefore, the penetrance and expressivity  
480 of the KV phenotype in *MZcarmil3<sup>stl413</sup>* mutants correlated well with those of the *spaw*  
481 asymmetric staining defect during mid-segmentation stages and the L/R heart positioning  
482 defect at the end of embryogenesis, consistent with the findings of Gokey and colleagues  
483 (Gokey et al., 2016) and Sampaio and colleagues (Sampaio et al., 2014).

## 484 Discussion

485 We investigated the role of the actin assembly regulator, CARMIL3, in cell migration and  
486 morphogenesis during early zebrafish development. First, we confirmed that in actin  
487 polymerization assays, human CARMIL3 and zebrafish *Carmil3* interact with and regulate the

488 activity of capping protein with respect to actin polymerization. More important, we discovered  
489 that *Carmil3* is required for normal migration of endodermal cells and the aggregation of  
490 dorsal forerunner cells (DFCs) during zebrafish gastrulation. Impaired aggregation of DFCs  
491 led to defects in the formation of the KV in terms of its shape and size. These KV defects  
492 were associated with decreased numbers of cilia present in mutant KVs; as a consequence,  
493 L/R asymmetry was impaired, manifested by malposition of the marker *spaw* during  
494 segmentation and later in the position of the zebrafish heart tube. These KV and L/R  
495 phenotypes displayed variable but correlated penetrance and expressivity.

496 The two *carmil3* mutant alleles we report here were generated by reverse genetic  
497 approaches: *carmil3*<sup>sa19830</sup> by TILLING for ENU-induced nonsense mutations (Kettleborough  
498 et al., 2013) and *carmil*<sup>stl413</sup> by deploying TAL endonucleases (Boch et al., 2009; Moscou and  
499 Bogdanove, 2009). Both are premature stop codons predicted to produce truncated proteins  
500 and thus should represent strong or null alleles. Consistent with that view, the phenotypes  
501 are recessive. However, our study does not include an analysis of the protein products that  
502 would test this view definitively. The observation that only maternal zygotic but not zygotic  
503 *carmil3* mutants presented gastrulation phenotypes, is consistent with known significant  
504 maternal *carmil3* expression, which is likely to compensate for the lack of zygotic expression  
505 during gastrulation (Solnica-Krezel, 2020; Stark and Cooper, 2015). The lack of full  
506 penetrance for the later phenotypes indicates a substantial level of robustness in the  
507 processes of cell migration and morphogenesis, consistent with observations for many other  
508 genes regulating early embryogenesis (Chen et al., 2018; Kelly et al., 2000; Li-Villarreal et al.,  
509 2015; Solnica-Krezel and Driever, 2001). CARMILs are encoded by three conserved genes in  
510 vertebrates, including zebrafish, so redundant and overlapping functions contributed by  
511 CARMIL1 or CARMIL2 may also account for the variable level of penetrance seen for  
512 downstream phenotypes. In addition, as the two *carmil3* mutant alleles are nonsense  
513 mutations, the observed phenotypes could represent only partial loss-of-function and  
514 variability due to genetic compensation triggered by RNA degradation (El-Brolosy et al.,  
515 2019; Ma et al., 2019).

516 Our results provide new information about the function of CARMIL3, especially in the *in*  
517 *vivo* context of a whole vertebrate organism during the process of embryogenesis. Previous  
518 studies on CARMIL3 have used cell culture and mouse tumor models to uncover roles in  
519 neuronal synapse formation and cancer cell migration, based on actin assembly (Hsu et al.,  
520 2011; Lanier et al., 2016; Spence et al., 2019; Wang et al., 2020).

521 Previous studies, with human cultured cells that express both CARMIL1 and CARMIL2,  
522 found overlapping but distinct functions for the two proteins, based on subcellular localization  
523 and knockdown phenotypes (Liang et al., 2009; Stark et al., 2017). While the early  
524 phenotypes observed here display strong penetrance, the later phenotypes are far less  
525 penetrant, raising the question of compensatory and overlapping function among the  
526 CARMIL-encoding genes. In support of the view, preliminary observations in our laboratories  
527 have revealed stronger L/R asymmetry phenotypes in double mutant zebrafish embryos that  
528 carry mutations in genes for both CARMIL2 and CARMIL3 (Stark, Solnica-Krezel and  
529 Cooper, 2019, unpublished); these observations will merit further study in the future.

530 We discovered that Carmil3 is important for the migration of endodermal cells during  
531 zebrafish gastrulation. Mutant endodermal cells had both reduced overall motility as well as  
532 reduced persistence. Recent work demonstrated cultured cells lacking CARMIL3 had  
533 reduced migration in the classical scratch assay and in trans-well migration. KO cells were  
534 less polarized, had less polymerized actin and fewer focal adhesions (Wang et al., 2020).  
535 Interestingly, the Rac-specific guanine nucleotide exchange factor, Prex1, was implicated in  
536 regulation of Nodal-dependent actin dynamics and random endoderm cell motility during  
537 gastrulation (Woo et al., 2012). Future experiments will determine if endodermal migration  
538 defects in *MZcarmil3* mutants are associated with abnormal actin organization and/or focal  
539 adhesion formation.

540 We found that Carmil3 is important for the aggregation of DFCs during gastrulation.  
541 DFCs typically migrate vegetalward ahead of the germ layers in one cluster of cells.  
542 Occasionally a few cells may separate from the cluster. DFC coalescence and migration as a  
543 cohesive cluster is strongly dependent on cell-cell adhesion. *cdh1*/E-cadherin  
544 (*halfbaked/volcano*) mutants in which cell adhesion is reduced, exhibit delayed epiboly of all  
545 germ layers and frequently fragmented DFC clusters (Shimizu et al., 2005; Solnica-Krezel et  
546 al., 1996). A recent study showed loss of CARMIL3 in cultured cells inhibits cadherin based  
547 adhesion through transcriptional downregulation of epidermal type gene expression (Wang et  
548 al., 2020). Such a mechanism might account for the reduced adhesion of DFC *in vivo*. We  
549 observed small and malformed KV, likely the direct result of the smaller DFC clusters.  
550 However, we cannot exclude a more direct role of Carmil3 in KV morphogenesis.

551 CARMILs appear to regulate actin via direct biochemical interactions with and effects on  
552 the actin-capping properties of CP (Edwards et al., 2013; Lanier et al., 2015; Stark et al.,

553 2017). Indeed, CP itself is known to have an important role in morphogenesis. Mutations in  
554 humans and in zebrafish of the gene encoding the beta subunit of CP, known as *capzb* in  
555 zebrafish, were found to cause craniofacial and muscle developmental defects, with effects  
556 on cell morphology, cell differentiation and neural crest migration (Mukherjee et al., 2016). In  
557 addition, the same study found that *capzb* overexpression produced embryonic lethality.

558         Among regulators of CP, CARMILs are only one family of proteins with CPI motifs.  
559 Among other CPI-motif protein families, which are unrelated to each other outside of their CPI  
560 motifs, several have been shown to have roles in actin-based processes of development. The  
561 CPI-motif protein CKIP-1 is important for myoblast fusion in mammalian and zebrafish  
562 systems (Baas et al., 2012). CapZIP, known as *duboraya/dub* in zebrafish, is important in  
563 zebrafish development for actin organization in cells lining the KV, cilia formation in the KV,  
564 and L/R asymmetry (Oishi et al., 2006). CD2AP, encoded by *cd2ap* in zebrafish, is important  
565 for the development and function of the kidney glomerulus, in mammals and zebrafish  
566 (Hentschel et al., 2007; Tossidou et al., 2019). Zebrafish CIN85, a homologue of CD2AP  
567 encoded by the gene *sh3kb1*, is also important for glomerular podocyte function (Teng et al.,  
568 2016), and it has a role in the formation and maintenance of the vascular lumen (Zhao and  
569 Lin, 2013). Finally, the twinfilin family of CPI-motif proteins, encode by four genes in zebrafish  
570 - *twf1a*, *twf1b*, *twf2a* and *twf2b*, has not been as well-studied, but may also affect actin  
571 assembly, as may the WASHCAP / Fam21 family of CPI-motif proteins, encoded by *washc2c*  
572 in zebrafish.

573         The *carmil3* mutant lines generated here provide a valuable tool for studying the  
574 regulation of actin dynamics during endoderm migration and KV morphogenesis in the  
575 context of a developing vertebrate embryo, and for testing potential functional interactions  
576 with CARMIL3 interacting proteins.

## 577 Acknowledgments

578         We are grateful to members of our laboratories for advice and assistance. We are  
579 grateful for the activities and support of the Washington University Zebrafish Facility and the  
580 University of Iowa Zebrafish Facility. This research was supported by the following grants:  
581 NIH R35 GM118171 to JAC, and NIH R35 GM118179 to LSK.

## 582 References

- 583 Ahmad, N., Long, S., Rebagliati, M., 2004. A Southpaw Joins the Roster: The Role of the  
584 Zebrafish *Nodal-Related Gene Southpaw* in Cardiac LR Asymmetry. *Trends Cardiovasc.*  
585 *Med.* 14, 43-49.
- 586 Alexander, J., Rothenberg, M., Henry, G.L., Stainier, D.Y., 1999. *casanova* Plays an Early  
587 and Essential Role in Endoderm Formation in Zebrafish. *Dev. Biol.* 215, 343-357.
- 588 Amack, J.D., 2014. Salient features of the ciliated organ of asymmetry. *Bioarchitecture* 4, 6-  
589 15.
- 590 Amack, J.D., Wang, X., Yost, H.J., 2007. Two T-box genes play independent and cooperative  
591 roles to regulate morphogenesis of ciliated Kupffer's vesicle in zebrafish. *Dev. Biol.* 310,  
592 196-210.
- 593 Amack, J.D., Yost, H.J., 2004. The T box transcription factor no tail in ciliated cells controls  
594 zebrafish left-right asymmetry. *Curr. Biol.* 14, 685-690.
- 595 Baas, D., Caussanel-Boude, S., Guiraud, A., Calhabeu, F., Delaune, E., Pilot, F., Chopin, E.,  
596 Machuca-Gayet, I., Vernay, A., Bertrand, S., Rual, J.F., Jurdic, P., Hill, D.E., Vidal, M.,  
597 Schaeffer, L., Goillot, E., 2012. CKIP-1 regulates mammalian and zebrafish myoblast  
598 fusion. *J. Cell Sci.* 125, 3790-3800.
- 599 Boch, J., Scholze, H., Schornack, S., Landgraf, A., Hahn, S., Kay, S., Lahaye, T., Nickstadt,  
600 A., Bonas, U., 2009. Breaking the Code of DNA binding Specificity of TAL-type III  
601 Effectors. *Science* 326, 1509-1512.
- 602 Carlsson, A.E., Wear, M.A., Cooper, J.A., 2004. End versus Side Branching by Arp2/3  
603 Complex. *Biophys. J.* 86, 1074-1081.
- 604 Chen, J., Castelveccchi, G.D., Li-Villarreal, N., Raught, B., Krezel, A.M., McNeill, H., Solnica-  
605 Krezel, L., 2018. Atypical Cadherin Dachous1b Interacts with Ttc28 and Aurora B to  
606 Control Microtubule Dynamics in Embryonic Cleavages. *Dev. Cell* 45, 376-391.e5.
- 607 Edwards, M., Liang, Y., Kim, T., Cooper, J.A., 2013. Physiological role of the interaction  
608 between CARMIL1 and capping protein. *Mol. Biol. Cell* 24, 3047-3055.
- 609 Edwards, M., Zwolak, A., Schafer, D.A., Sept, D., Dominguez, R., Cooper, J.A., 2014.  
610 Capping protein regulators fine-tune actin assembly dynamics. *Nat. Rev. Mol. Cell Biol.*  
611 15, 677-689.
- 612 El-Brolosy, M.A., Kontarakis, Z., Rossi, A., Kuenne, C., Günther, S., Fukuda, N., Kikhi, K.,  
613 Boezio, G.L.M., Takacs, C.M., Lai, S.L., Fukuda, R., Gerri, C., Giraldez, A.J., Stainier,  
614 D.Y.R., 2019. Genetic compensation triggered by mutant mRNA degradation. *Nature*  
615 568, 193-197.
- 616 Gokey, J.J., Dasgupta, A., Amack, J.D., 2015. The V-ATPase accessory protein Atp6ap1b  
617 mediates dorsal forerunner cell proliferation and left-right asymmetry in zebrafish. *Dev.*  
618 *Biol.* 407, 115-130.
- 619 Gokey, J.J., Ji, Y., Tay, H.G., Litts, B., Amack, J.D., 2016. Kupffer's Vesicle Size Threshold  
620 for Robust Left-Right Patterning of the Zebrafish Embryo. *Dev. Dyn.* 245, 22-33.
- 621 Hentschel, D.M., Mengel, M., Boehme, L., Liebsch, F., Albertin, C., Bonventre, J.V., Haller,  
622 H., Schiffer, M., 2007. Rapid screening of glomerular slit diaphragm integrity in larval  
623 zebrafish. *Am. J. Physiol. Renal Physiol.* 293, F1746-50.
- 624 Hsu, C.C., Chiang, C.W., Cheng, H.C., Chang, W.T., Chou, C.Y., Tsai, H.W., Lee, C.T., Wu,  
625 Z.H., Lee, T.Y., Chao, A., Chow, N.H., Ho, C.L., 2011. Identifying LRRC16B as an  
626 oncofetal gene with transforming enhancing capability using a combined bioinformatics  
627 and experimental approach. *Oncogene* 30, 654-667.
- 628 Hu, B., Gao, Y., Davies, L., Woo, S., Topczewski, J., Jessen, J.R., Lin, F., 2018. Glypican 4  
629 and Mmp14 interact in regulating the migration of anterior endodermal cells by limiting  
630 extracellular matrix deposition. *Development* 145, dev163303.

- 631 Johnson, B., McConnell, P., Kozlov, A.G., Mekel, M., Lohman, T.M., Gross, M.L.,  
632 Amarasinghe, G.K., Cooper, J.A., 2018. Allosteric Coupling of CARMIL and V-1 Binding  
633 to Capping Protein Revealed by Hydrogen-Deuterium Exchange. *Cell Rep.* 23, 2795-  
634 2804.
- 635 Kelly, C., Chin, A.J., Leatherman, J.L., Kozlowski, D.J., Weinberg, E.S., 2000. Maternally  
636 controlled  $\beta$ -catenin-mediated signaling is required for organizer formation in the  
637 zebrafish. *Development* 127, 3899-3911.
- 638 Kettleborough, R.N., Busch-Nentwich, E.M., Harvey, S.A., Dooley, C.M., de Bruijn, E., van  
639 Eeden, F., Sealy, I., White, R.J., Herd, C., Nijman, I.J., Fényes, F., Mehroke, S., Scahill,  
640 C., Gibbons, R., Wali, N., Carruthers, S., Hall, A., Yen, J., Cuppen, E., Stemple, D.L.,  
641 2013. A systematic genome-wide analysis of zebrafish protein-coding gene function.  
642 *Nature* 496, 494-497.
- 643 Kimmel, C.B., Ballard, W.W., Kimmel, S.R., Ullmann, B., Schilling, T.F., 1995. Stages of  
644 Embryonic Development of the Zebrafish. *Dev. Dyn.* 203, 253-310.
- 645 Lanier, M.H., Kim, T., Cooper, J.A., 2015. CARMIL2 is a novel molecular connection between  
646 vimentin and actin essential for cell migration and invadopodia formation. *Mol. Biol. Cell*  
647 26, 4577-4588.
- 648 Lanier, M.H., McConnell, P., Cooper, J.A., 2016. Cell Migration and Invadopodia Formation  
649 Require a Membrane-binding Domain of CARMIL2. *J. Biol. Chem.* 291, 1076-1091.
- 650 Li-Villarreal, N., Forbes, M.M., Loza, A.J., Chen, J., Ma, T., Helde, K., Moens, C.B., Shin, J.,  
651 Sawada, A., Hindes, A.E., Dubrulle, J., Schier, A.F., Longmore, G.D., Marlow, F.L.,  
652 Solnica-Krezel, L., 2015. Dachous1b cadherin regulates actin and microtubule  
653 cytoskeleton during early zebrafish embryogenesis. *Development* 142, 2704-2718.
- 654 Liang, Y., Niederstrasser, H., Edwards, M., Jackson, C.E., Cooper, J.A., 2009. Distinct Roles  
655 for CARMIL Isoforms in Cell Migration. *Mol. Biol. Cell* 20, 5290-5305.
- 656 Lin, F., Sepich, D.S., Chen, S., Topczewski, J., Yin, C., Solnica-Krezel, L., Hamm, H., 2005.  
657 Essential roles of  $G\alpha_{12/13}$  signaling in distinct cell behaviors driving zebrafish  
658 convergence and extension gastrulation movements. *J. Cell Biol.* 169, 777-787.
- 659 Long, S., Ahmad, N., Rebagliati, M., 2003. The zebrafish *nodal*-related gene *southpaw* is  
660 required for visceral and diencephalic left-right asymmetry. *Development* 130, 2303-  
661 2316.
- 662 Ma, Z., Zhu, P., Shi, H., Guo, L., Zhang, Q., Chen, Y., Chen, S., Zhang, Z., Peng, J., Chen,  
663 J., 2019. PTC-bearing mRNA elicits a genetic compensation response via Upf3a and  
664 COMPASS components. *Nature* 568, 259-263.
- 665 Mizoguchi, T., Verkade, H., Heath, J.K., Kuroiwa, A., Kikuchi, Y., 2008. Sdf1/Cxcr4 signaling  
666 controls the dorsal migration of endodermal cells during zebrafish gastrulation.  
667 *Development* 135, 2521-2529.
- 668 Moscou, M.J., Bogdanove, A.J., 2009. A Simple Cipher Governs DNA recognition by TAL  
669 Effectors. *Science* 326, 1501.
- 670 Mukherjee, K., Ishii, K., Pillalamarri, V., Kammin, T., Atkin, J.F., Hickey, S.E., Xi, Q.J.,  
671 Zepeda, C.J., Gusella, J.F., Talkowski, M.E., Morton, C.C., Maas, R.L., Liao, E.C., 2016.  
672 Actin capping protein CAPZB regulates cell morphology, differentiation, and neural crest  
673 migration in craniofacial morphogenesis. *Hum. Mol. Genet.* 25, 1255-1270.
- 674 Neugebauer, J.M., Yost, H.J., 2014. FGF signaling is required for brain left-right asymmetry  
675 and brain midline formation. *Dev. Biol.* 386, 123-134.
- 676 Oishi, I., Kawakami, Y., Raya, A., Callol-Massot, C., Izpisua Belmonte, J.C., 2006. Regulation  
677 of primary cilia formation and left-right patterning in zebrafish by a noncanonical Wnt  
678 signaling mediator, *duboraya*. *Nat. Genet.* 38, 1316-1322.
- 679 Oteíza, P., Köppen, M., Concha, M.L., Heisenberg, C.P., 2008. Origin and shaping of the  
680 laterality organ in zebrafish. *Development* 135, 2807-2813.



- 681 Panizzi, J.R., Jessen, J.R., Drummond, I.A., Solnica-Krezel, L., 2007. New functions for a  
682 vertebrate Rho guanine nucleotide exchange factor in ciliated epithelia. *Development*  
683 134, 921-931.
- 684 Pézeron, G., Mourrain, P., Courty, S., Ghislain, J., Becker, T.S., Rosa, F.M., David, N.B.,  
685 2008. Live analysis of endodermal layer formation identifies random walk as a novel  
686 gastrulation movement. *Curr. Biol.* 18, 276-281.
- 687 Piperno, G., Fuller, M.T., 1985. Monoclonal Antibodies Specific for an Acetylated Form of  $\alpha$ -  
688 Tubulin Recognize the Antigen in Cilia and Flagella from a Variety of Organisms. *J. Cell*  
689 *Biol.* 101, 2085-2094.
- 690 Ramabhadran, V., Gurel, P.S., Higgs, H.N., 2012. Mutations to the Formin Homology 2  
691 Domain of INF2 protein have Unexpected Effects on Actin Polymerization and Severing.  
692 *J. Biol. Chem.* 287, 34234-34245.
- 693 Sampaio, P., Ferreira, R.R., Guerrero, A., Pintado, P., Tavares, B., Amaro, J., Smith, A.A.,  
694 Montenegro-Johnson, T., Smith, D.J., Lopes, S.S., 2014. Left-Right Organizer Flow  
695 Dynamics: How Much Cilia Activity Reliably Yields Laterality? *Dev. Cell* 29, 716-728.
- 696 Schmid, B., Shah, G., Scherf, N., Weber, M., Thierbach, K., Campos, C.P., Roeder, I.,  
697 Aanstad, P., Huisken, J., 2013. High-speed panoramic light-sheet microscopy reveals  
698 global endodermal cell dynamics. *Nat. Commun.* 4, 2207.
- 699 Schneider, C.A., Rasband, W.S., Eliceiri, K.W., 2012. NIH Image to ImageJ: 25 years of  
700 Image Analysis. *Nat. Methods* 9, 671-675.
- 701 Shimizu, T., Yabe, T., Muraoka, O., Yonemura, S., Aramaki, S., Hatta, K., Bae, Y.K., Nojima,  
702 H., Hibi, M., 2005. E-cadherin is required for gastrulation cell movements in zebrafish.  
703 *Mech. Dev.* 122, 747-763.
- 704 Solnica-Krezel, L., 2020. Maternal contributions to gastrulation in zebrafish. *Curr. Top. Dev.*  
705 *Biol.* 140, 391-427.
- 706 Solnica-Krezel, L., Driever, W., 2001. The role of the homeodomain protein Bozozok in  
707 Zebrafish axis formation. *Int. J. Dev. Biol.* 45, 299-310.
- 708 Solnica-Krezel, L., Stemple, D.L., Mountcastle-Shah, E., Rangini, Z., Neuhauss, S.C.,  
709 Malicki, J., Schier, A.F., Stainier, D.Y., Zwartkruis, F., Abdelilah, S., Driever, W., 1996.  
710 Mutations affecting cell fates and cellular rearrangements during gastrulation in  
711 zebrafish. *Development* 123, 67-80.
- 712 Spence, E.F., Dube, S., Uezu, A., Locke, M., Soderblom, E.J., Soderling, S.H., 2019. In vivo  
713 proximity proteomics of nascent synapses reveals a novel regulator of cytoskeleton-  
714 mediated synaptic maturation. *Nat. Commun.* 10, 386.
- 715 Stark, B.C., Cooper, J.A., 2015. Differential Expression of CARMIL-Family Genes During  
716 Zebrafish Development. *Cytoskeleton (Hoboken)* 72, 534-541.
- 717 Stark, B.C., Lanier, M.H., Cooper, J.A., 2017. CARMIL family proteins as multidomain  
718 regulators of actin-based motility. *Mol. Biol. Cell* 28, 1713-1723.
- 719 Teng, B., Schroder, P., Müller-Deile, J., Schenk, H., Staggs, L., Tossidou, I., Dikic, I., Haller,  
720 H., Schiffer, M., 2016. CIN85 Deficiency Prevents Nephrin Endocytosis and Proteinuria  
721 in Diabetes. *Diabetes* 65, 3667-3679.
- 722 Thisse, C., Thisse, B., 2008. High-resolution *in situ* hybridization to whole-mount zebrafish  
723 embryos. *Nat. Protoc.* 3, 59-69.
- 724 Topczewski, J., Sepich, D.S., Myers, D.C., Walker, C., Amores, A., Lele, Z., Hammerschmidt,  
725 M., Postlethwait, J., Solnica-Krezel, L., 2001. The Zebrafish Glypican Knypek Controls  
726 Cell Polarity during Gastrulation Movements of Convergent Extension. *Dev. Cell* 1, 251-  
727 264.
- 728 Tossidou, I., Teng, B., Worthmann, K., Müller-Deile, J., Jobst-Schwan, T., Kardinal, C.,  
729 Schroder, P., Bolanos-Palmieri, P., Haller, H., Willerding, J., Drost, D.M., de Jonge, L.,  
730 Reubold, T., Eschenburg, S., Johnson, R.I., Schiffer, M., 2019. Tyrosine

- 731            Phosphorylation of CD2AP Affects Stability of the Slit Diaphragm Complex. *J. Am. Soc.*  
732            *Nephrol.* 30, 1220-1237.
- 733            Wang, H., Wang, C., Peng, G., Yu, D., Cui, X.G., Sun, Y.H., Ma, X., 2020. Capping Protein  
734            Regulator and Myosin 1 Linker 3 Is Required for Tumor Metastasis. *Mol. Cancer Res.*  
735            18, 240-252.
- 736            Warga, R.M., Kimmel, C.B., 1990. Cell movements during epiboly and gastrulation in  
737            zebrafish. *Development* 108, 569-580.
- 738            Woo, S., Housley, M.P., Weiner, O.D., Stainier, D.Y., 2012. Nodal signaling regulates  
739            endodermal cell motility and actin dynamics via Rac1 and Prex1. *J. Cell Biol.* 198, 941-  
740            952.
- 741            Xu, H., Echemendia, N., Chen, S., Lin, F., 2011. Identification and Expression Patterns of  
742            Members of the Protease-Activated Receptor (PAR) Gene Family During Zebrafish  
743            Development. *Dev. Dyn.* 240, 278-287.
- 744            Ye, D., Lin, F., 2013. S1pr2/G $\alpha_{13}$  signaling controls myocardial migration by regulating  
745            endoderm convergence. *Development* 140, 789-799.
- 746            Ye, D., Xie, H., Hu, B., Lin, F., 2015. Endoderm convergence controls subduction of the  
747            myocardial precursors during heart-tube formation. *Development* 142, 2928-2940.
- 748            Yelon, D., Horne, S.A., Stainier, D.Y., 1999. Restricted Expression of Cardiac Myosin Genes  
749            Reveals Regulated Aspects of Heart Tube Assembly in Zebrafish. *Dev. Biol.* 214, 23-37.
- 750            Zhao, Y., Lin, S., 2013. Essential Role of SH3-domain GRB2-like 3 for Vascular Lumen  
751            Maintenance in Zebrafish. *Arterioscler. Thromb. Vasc. Biol.* 33, 1280-1286.

752

753 **Tables.**

754 Table I. Pattern of expression of *spaw* at 18-20 somites, comparing *carmil3* maternal zygotic  
755 (MZ) mutant embryos with WT embryos. The percentage of the total number of embryos with  
756 different patterns are listed, along with 95% confidence intervals (CI) and the number of  
757 embryos scored (N). Statistics, including confidence intervals, were calculated with GraphPad  
758 Prism.

759

Genotype	Phenotypic Pattern, Percent of Total (95% CI)				N
	Left	Right	Bilateral	Absent	
Wild type	98 (94–99)	1 (0–3)	2 (0–5)	0	172
MZ <i>carmil3</i> <sup>stl413</sup>	54 (46–62)	9 (5–15)	26 (20–34)	11 (7–17)	137
MZ <i>carmil3</i> <sup>sa19830</sup>	53 (43–64)	7 (3–14)	31 (22–41)	9 (5–17)	88

760

761

762